Hindawi
Shock and Vibration
Volume 2022, Article ID 2703789, 16 pages
https://doi.org/10.1155/2022/2703789

Research Article

Error-Index-Based Algorithm for Low-Velocity Impact Localization

Tao Peng,[1,2] **Lilin Cui**,[1,2] **Xiufeng Huang**,[1,2] **Wenjing Yu**,[1,2] **and Rongwu Xu**[1,2]

[1]*National Key Laboratory on Ship Vibration and Noise, Naval University of Engineering, Wuhan 430033, China*
[2]*Institute of Noise and Vibration, Naval University of Engineering, Wuhan 430033, China*

Correspondence should be addressed to Wenjing Yu; ywjada@163.com

Received 27 May 2022; Accepted 12 August 2022; Published 8 September 2022

Academic Editor: Zhixiong Li

Flat plates and cylindrical shells are commonly used in large equipment. To locate the low-velocity impact points in these structures, this study proposes an error-index-based algorithm for impact localization. The time of arrival of an impact-generated A0 Lamb waves was first estimated based on the energy of the signal. Equations for calculating the error indices were proposed for flat-plate and cylindrical shell structures, and the probability distribution functions of the impact points are constructed for visual localization. The impact test results on a flat plate and cylindrical shell indicated that, compared to the Morlet wavelet method, the proposed algorithm improved the mean relative error of impact point localization on the flat plate by 0.22%, 15.64%, and 15.26% under three different noise conditions, respectively (i.e., no noise, and SNR = 5 and 0 dB). For the cylindrical shell, the mean relative error of impact localization improved by 1.8%, 3.97%, and 28.12% under the three conditions, respectively. The results indicated that the proposed localization algorithm can accurately locate the impact points on a flat plate and cylindrical shell, even under strong background noise conditions, providing a reference for future research on locating low-velocity impact points in large equipment.

1. Introduction

In recent years, impact localization in large equipment has become a research hotspot in the field of structural health monitoring. Impact events, including high- and low-velocity events, often damage equipment. In general, the damage caused by high-velocity impact events is visible impact damage, whereas low-velocity impact can cause barely visible impact damage (BVID), posing a serious threat to the operational safety of the equipment [1, 2]. Events, such as the sudden fall of a component or an unexpected hit from a foreign object, can cause impact damage to the equipment. Therefore, it is critical to find the impact location in time to detect the impact damage, facilitate timely inspection and repair, reduce economic loss, and prevent major accidents [3, 4].

Current research mainly adopts two approaches for low-velocity impact localization in large structures. The first approach is based on feature extraction, such as using the time of arrival (TOA) or amplitude of the signal received from the sensor, for impact localization [5, 6]. The most common method utilizes trigonometric identities, where the impact location is determined based on the distance, TOA, and wave velocity [7, 8]. Ciampa and Meo [9] proposed an improved trigonometry-based algorithm for impact localization in isotropic materials, which does not require the wave velocity but only the TOA. Some of the common methods for TOA estimation include threshold selection [10], wavelet transform [11–13], and cross-correlation [2, 14, 15]. In addition, beamforming [16] and the time-reversal focusing technique [17] have been used for impact localization. Papulak [18] proposed a one-dimensional beamforming localization algorithm. Impact tests were performed on a large structure (6.04 m^2) using a one-dimensional sensor array, and good localization results were achieved. He et al. [19] located the impacts from dual sources using both beamforming and singular value decomposition. Qiu et al. [20] extracted the phase velocity of a stress wave

through wavelet transform and achieved visual localization of a reinforced plate with the time-reversal focusing technique. Pang et al. [21] estimated the TOA by extracting stress waves through wavelet transforms and achieved localization using the centroid method.

The second approach is data-driven, in which a known set of features of the impact signal are generally mapped to the impact locations using a training algorithm. Such methods include database matching [22, 23] and machine-learning-based methods [24, 25]. The database matching method requires impact testing at different locations on the structure surface in advance to build a characteristics database of elastic waves generated at different impact points. The elastic wave characteristics generated by the actual impact are matched with the database, and the location with the highest matching degree is selected as the impact location. Many studies have used artificial neural networks for impact localization. The best localization performance was achieved when the TOA features were applied as input to the neural network [26]. Other frequently used features include the signal amplitude and the time corresponding to the signal amplitude [27].

However, both methods have their own limitations. In feature- extraction-based methods, it is difficult to accurately extract the signal TOA due to dispersion effects [28] and interference from noise and complex reinforced structures during wave propagation. Data-driven methods require a reference database; for large structures, this demands large initial investment for building the database, and operation is inconvenient.

To address the limitations of these methods, this study proposes an impact localization method based on the error index, which does not require a reference database and can achieve localization even under the interference of strong noise. A simple and fast dual-root mean square (RMS) algorithm is first used to estimate the TOA, and the probability distribution functions are established based on the time difference of arrival (TDOA) for visualization. Impact tests are performed on a flat plate and cylindrical shell, which are commonly used in large equipment. The test results indicate that the proposed algorithm can accurately locate the impact points on the flat plate and cylindrical shell under strong background noise conditions.

2. Error-Index-Based Impact Localization Algorithm

2.1. Localization on an Isotropic Plate. Elastic wave propagation occurs when the equipment surface or internal structure is impacted. These waves can be categorized into longitudinal waves, transverse waves, Rayleigh waves, A0 Lamb waves, and others, and can be captured by various sensors on the surface of the structure. As longitudinal, transverse, and Rayleigh waves have small amplitudes compared to A0 Lamb waves, many studies utilize the properties of A0 Lamb waves for impact localization [29, 30].

Most of the materials used in the construction of large equipment, such as nuclear power plants and ships, are steel. Steel plates can be generally considered isotropic [31]. As shown in Figure 1, multiple sensors are arranged on a flat plate. When an impact event occurs, the A0 Lamb waves generated by the collision propagate in all directions. The A0 Lamb waves received by sensors at different distances from the impact location contain different information. In this figure, I denotes the impact point, S_i, S_j, S_m, S_n denote the sensors, and L_i, L_j, L_m, L_n denote the linear distance from the impact point to the respective sensors. The features of the signals received by the sensors are depicted in Figure 2. The signals reach the sensors at different time instants. As the travel distance increases, the signal amplitude decreases, and the waveform gradually changes, indicating dispersion effects during wave propagation [32].

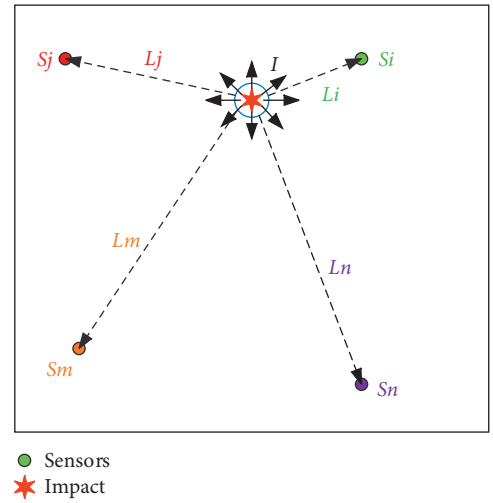

Figure 1: Wave propagation paths to the sensors on an isotropic plate.

It is assumed that an impact occurs at time t_0; the distance between the impact source and sensor is L; the propagation velocity of the A0 Lamb waves along different directions is V; the time of arrival of the A0 Lamb waves at the sensor is the TOA. The propagation process of the impact-wave can then be expressed as follows:

$$\begin{aligned} L_i &= V_i \times (TOA_i - t_0), \\ L_j &= V_j \times \left(TOA_j - t_0\right), \\ L_m &= V_m \times (TOA_m - t_0), \\ L_n &= V_n \times (TOA_n - t_0). \end{aligned} \tag{1}$$

It is difficult to determine when the impact exactly occurs (t_0). However, the wave propagation velocity is equal in different directions in an isotropic plate [33]. Therefore, we have

$$V_i = V_j = V_m = V_n = V. \tag{2}$$

Based on equations (1) and (2), we obtain

$$\begin{aligned} L_i - L_j &= V \times \left(\mathrm{TOA}_i - \mathrm{TOA}_j\right), \\ L_m - L_n &= V \times \left(\mathrm{TOA}_m - \mathrm{TOA}_n\right). \end{aligned} \tag{3}$$

Hence,

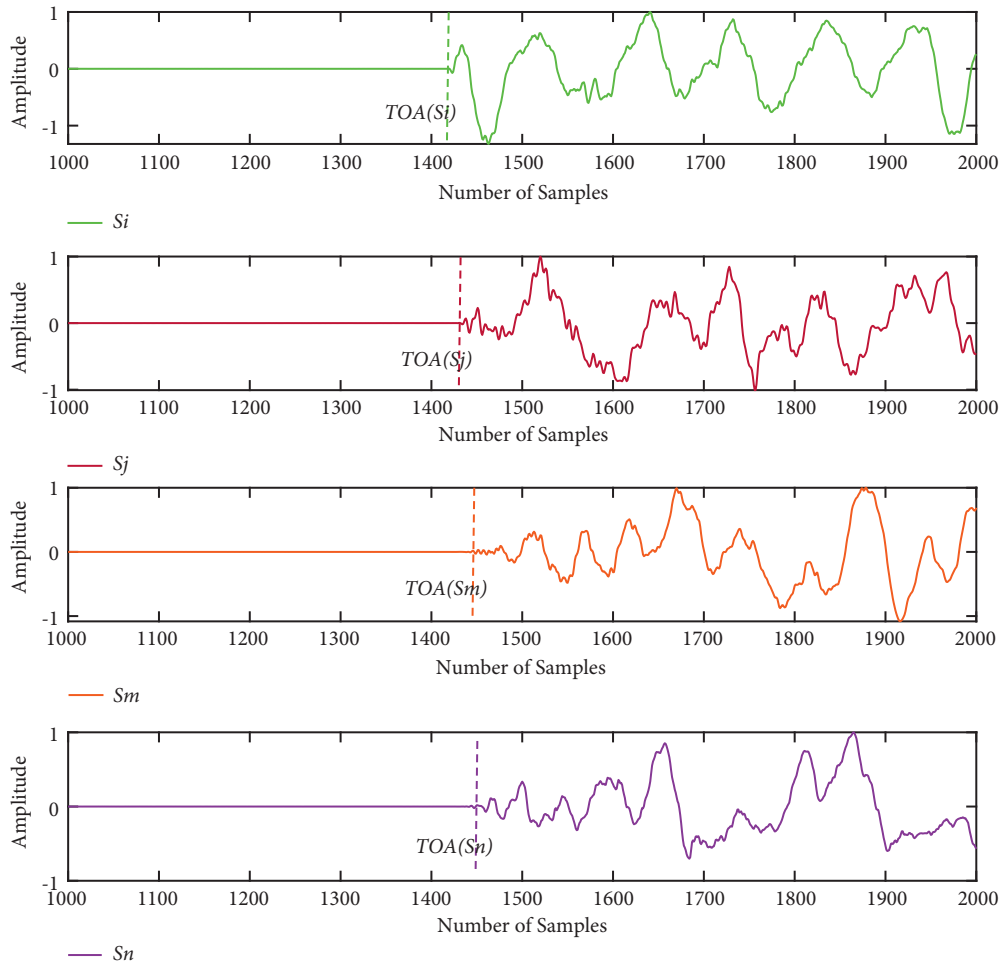

Figure 2: Impact signals received from the sensors.

$$V = \frac{L_i - L_j}{\left(\mathrm{TOA}_i - \mathrm{TOA}_j\right)} = \frac{L_m - L_n}{\left(\mathrm{TOA}_m - \mathrm{TOA}_n\right)}, \tag{4}$$

where $\mathrm{TOA}_i, \mathrm{TOA}_j, \mathrm{TOA}_m, \mathrm{TOA}_n$, denote the TOA of the A0 Lamb waves generated by impact on the different sensors.

2.2. Morlet Continuous Wavelet Algorithm for TOA Estimation. Morlet wavelet transform is a common signal processing method, in which Morlet wavelet changes are used to extract the arrival time of stress waves [21]. The complex Morlet continuous wavelet transform of signals is defined as follows:

$$WT(a,b) = \langle f, \varphi_{a,b} \rangle = -\frac{1}{\sqrt{a}} \int_R S(t) \overline{\varphi\left(\frac{t-b}{a}\right)} \mathrm{dt}, \tag{5}$$

where a is the stretching factor, b is the translation factor, and $\varphi(t)$ is the complex Morlet mother wavelet function given by

$$\varphi(t) = \frac{1}{\sqrt{\pi f_b}} e^{2i\pi f_c t} e^{-t^2/f_b}, \tag{6}$$

where f_c and f_b are the center frequency and bandwidth, respectively, of the female wavelet.

The Fourier transform of the complex Morlet continuous wavelet is

$$\Phi_{a,b}(\omega) = \sqrt{a} e^{-i\omega b} e^{(-1/2)(\omega_b/4\pi)(a\omega - w_c)^2}. \tag{7}$$

Based on equation (7), the complex Morlet continuous wavelet transform of the signal $S(t)$ represents the time-frequency component of the signal for time $t = b$, frequency $\omega = \omega_c/a$, and frequency band $\omega_1, \omega_2 \in [\omega_c/a - \omega_b/2a, \omega_c/a + \omega_b/2a]$. The scale factor a and wavelet bandwidth f_b are adjusted. The complex Morlet wavelet transform extracts the narrowband Lamb wave signal from the impact stress-wave signal, and then the modulus of the extracted signal is calculated. Subsequently, the peak value of the mode is taken as the arrival time of the impact stress wave.

However, this method needs to adjust the frequency parameters ω according to the positioning results, and the parameter Settings varies greatly for different scenes and materials, which complicates the actual positioning process. Moreover, while calculating for the TOA of the signal, Morlet wavelet transform is susceptible to noise interference, which is detrimental to impact positioning under actual

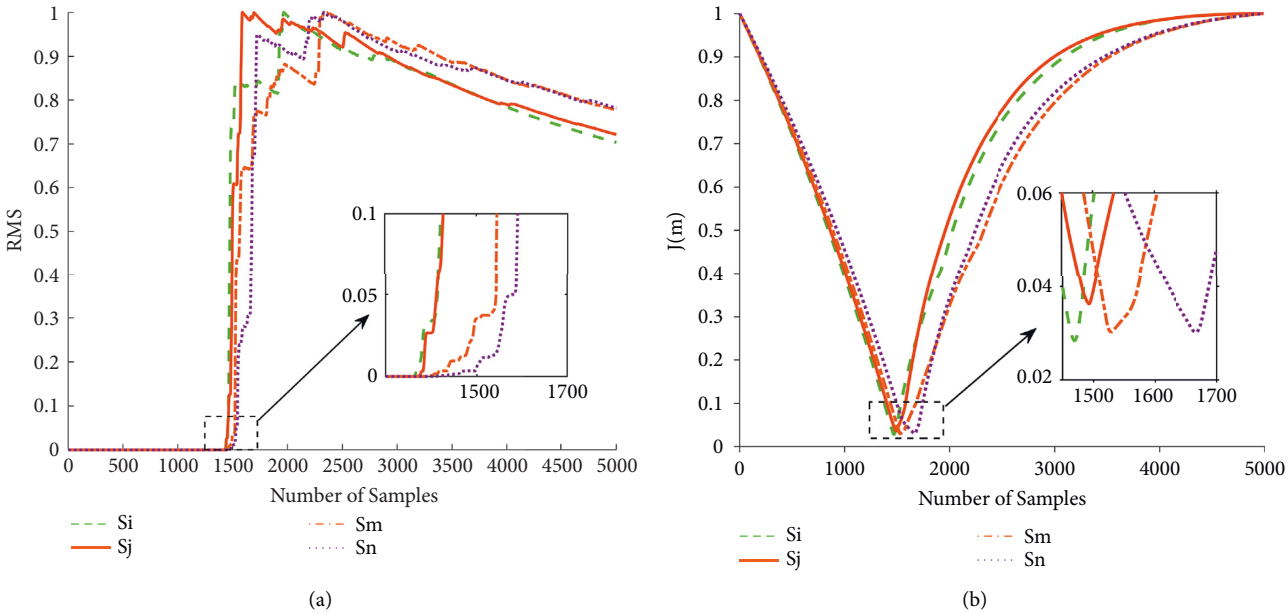

Figure 3: RMS curves of the signals received from the sensors. (a) RMS curves of different signals. (b) The total residual error $J(m)$ of different signals.

conditions. Therefore, this study proposes TOA extraction based on the RMS algorithm.

2.3. Dual-RMS Algorithm for TOA Estimation. Although the determination of the TOA of a A0 Lamb waves is crucial, the determination of the exact TOA requires complex signal processing considering the dispersion effects of the A0 Lamb waves and the interference of background noise. To automatically estimate the TOA of a A0 Lamb waves, this study proposes a simple and fast dual-RMS algorithm, which is described next.

First, the RMS of the signal is calculated as follows:

$$\mathrm{RMS}_{S_i}(n) = \sqrt{\frac{\sum_k^n S_i(k)^2}{n}} (n = 1, 2, \ldots, N), \tag{8}$$

where N is the number of samples of signal S_i, $S_i(k)$ is the amplitude of the k-th sampling point of signal S_i, and $\mathrm{RMS}_{S_i}(n)$ is the RMS value of signal S_i at the n-th sampling point.

The RMS curve of each signal is normalized, and the energy of each signal is calculated by taking the RMS of the signal. Then, the RMS curves for each signal are drawn, as shown in Figure 3. It can be observed that the RMS curve increases rapidly when the signal reaches the sensor. The traditional TOA extraction method involves the use of a fixed threshold. The time when the signal energy exceeds the predetermined threshold is considered the moment of arrival [29]. To a certain extent, the fixed-threshold approach is only suitable for certain working conditions, and when the external conditions change, it is difficult to accurately determine the TOA using this method. In this study, the statistical characteristics of the RMS curve of the signal are analyzed for adaptive TOA estimation. For signal S_i, the TOA is determined using the following procedure:

The signal energy curve is randomly divided into two parts, $\mathrm{RMS}_{S_i}(1{:}\ m)$ and $\mathrm{RMS}_{S_i}(m+1{:}\ N)$, with the m-th sampling point as the splitting point.

The empirical estimates (rms) of the two parts are calculated:

$$\begin{aligned} \mathrm{rms}_{S_i}(1{:}\ m) &= \frac{1}{m}\sum_{n=1}^{m}\left(\mathrm{RMS}_{S_i}(n)\right)^2, \\ \mathrm{rms}_{S_i}(m+1{:}\ N) &= \frac{1}{N-m}\sum_{n=m+1}^{N}\left(\mathrm{RMS}_{S_i}(n)\right)^2. \end{aligned} \tag{9}$$

The total residual error is calculated by accumulating the deviation from the empirical estimate for each point in each part [34]:

$$J_{S_i}(m) = \sum_{a=1}^{m}\left(\mathrm{RMS}_{S_i}(a) - \mathrm{rms}_{S_i}(1{:}\ m)\right)^2 + \sum_{b=m+1}^{N}\left(\mathrm{RMS}_{S_i}(b) - \mathrm{rms}_{S_i}(m+1{:}\ N)\right)^2. \tag{10}$$

The position of the splitting point is changed until the total residual $J_{S_i}(m)$ reaches a minimum, and this splitting point is considered the predicted time of arrival (PTOA).

Taking sensors S_i, S_j, S_m, S_n as an example, the RMS curve of each signal is shown in Figure 3(a), and the residual error J(m) of each point is obtained using equation (10), as

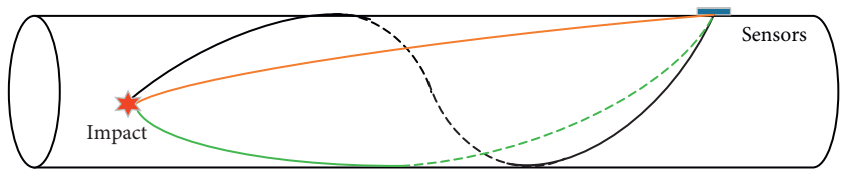

Figure 4: Multipath propagation of the impact signal to a sensor on a cylindrical shell.

shown in Figure 3(b). The minimum position of the J(m) curve in the figure represents the abrupt position change of the RMS curve, namely, the signal PTOA, which is mainly consistent with the signal TOA shown in Figure 3(a).

With the obtained PTOA_i, PTOA_j, PTOA_m, PTOA_n, we have

$$V = \frac{L_m - L_n}{L_i - L_j} = \frac{(\mathrm{TOA}_m - \mathrm{TOA}_n)}{(\mathrm{TOA}_i - \mathrm{TOA}_j)} = \frac{(\mathrm{PTOA}_m - \mathrm{PTOA}_n)}{(\mathrm{PTOA}_i - \mathrm{PTOA}_j)}. \tag{11}$$

Based on equations (4) and (11), the error index (E) is introduced for each pair of sensors as follows:

$$E = (L_i - L_j) \times (\mathrm{PTOA}_m - \mathrm{PTOA}_n) - (L_m - L_n) \times (\mathrm{PTOA}_i - \mathrm{PTOA}_j). \tag{12}$$

In the detection area, assuming that the coordinates of the impact source I are (X, Y), and the number of sensors is M, the error function $E(x, y)$ for any mesh point (x, y) in the detection area is

$$E(x,y) = \sum_{i=1}^{M}\sum_{j=1}^{M}\sum_{m=1}^{M}\sum_{n=1}^{M}\left|(L_i - L_j) \times (\mathrm{PTOA}_m - \mathrm{PTOA}_n) - (L_m - L_n) \times (\mathrm{PTOA}_i - \mathrm{PTOA}_j)\right|, \tag{13}$$

$$\begin{aligned} L_i &= \sqrt{(x - x_i)^2 + (y - y_i)^2}, \\ L_j &= \sqrt{(x - x_j)^2 + (y - y_j)^2}, \\ L_m &= \sqrt{(x - x_m)^2 + (y - y_m)^2}, \\ L_n &= \sqrt{(x - x_n)^2 + (y - y_n)^2}, \end{aligned} \tag{14}$$

where L_i, L_j, L_m, L_n denote the distance from mesh point (x, y) to different sensors.

The error is calculated for each mesh in the detection area, and a smaller error implies that the mesh point is closer to the actual impact source. The probability $P(x, y)$ that each mesh point is the impact source is calculated as follows:

$$P(x,y) = \frac{1}{E(x,y)/\min(E(x,y))} \times 100\%. \tag{15}$$

From the above equation, the mesh point with the largest $P(x, y)$ value is determined as the location of the impact source.

2.4. Localization on a Cylindrical Shell. Compared with the flat-plate structure, the cylindrical shell structure has the problem of multipath arrival signal superposition [35]. As shown in Figure 4, the impact-generated A0 Lamb waves will reach the sensor through multiple paths. Therefore, the shortest path from the impact signal to the sensor needs to be considered for impact localization in a cylindrical shell.

In cylindrical coordinates, the shortest path is calculated using equation (16). When calculating the distance between the mesh point of the cylindrical shell and the sensor, it is necessary to determine whether the angle difference $|\theta_i - \theta_s|$ between the two points is greater than π. If it is greater than π, the angle difference between the two points is $|2\pi - |\theta_i - \theta_s||$. The calculation is as follows:

$$L = \begin{cases} \sqrt{(|\theta_i - \theta_s| \times r)^2 + (Z_i - Z_s)^2}, & |\theta_i - \theta_s| \le \pi, \\ \sqrt{(|2\pi - |\theta_i - \theta_s|| \times r)^2 + (Z_i - Z_s)^2}, & |\theta_i - \theta_s| > \pi, \end{cases} \tag{16}$$

where θ_i and θ_s denote the angular coordinates of the i-th mesh point of the cylindrical shell and sensor S, respectively; Z_i and Z_s denote the axial coordinates of the i-th mesh point of the cylindrical shell and sensor S, respectively; and r is the radius of the cylindrical shell.

The impact localization algorithm for the cylindrical shell is consistent with that for the flat plate. The dual-RMS algorithm is used to determine the PTOA of the A0 Lamb waves for each signal, and the impact points are located using equations (14) and (15).

2.5. Relative Localization Error. Apart from the absolute error, the relative error is often established based on the dimensions of the structure under impact. Hence, for a large structure, the absolute localization error may be large, but as long as the relative localization error is within a reasonable range, the requirements for impact localization can be satisfied. Therefore, for the flat-plate structure, the relative error is defined as follows:

$$L\_\mathrm{Error} = \frac{\Delta L}{\sqrt{X^2 + Y^2}} \times 100\%, \tag{17}$$

where ΔL is the absolute distance between the predicted impact point and the actual impact point, and X and Y are the length and width of the flat plate, respectively.

For the cylindrical shell structure, the relative localization error is defined as

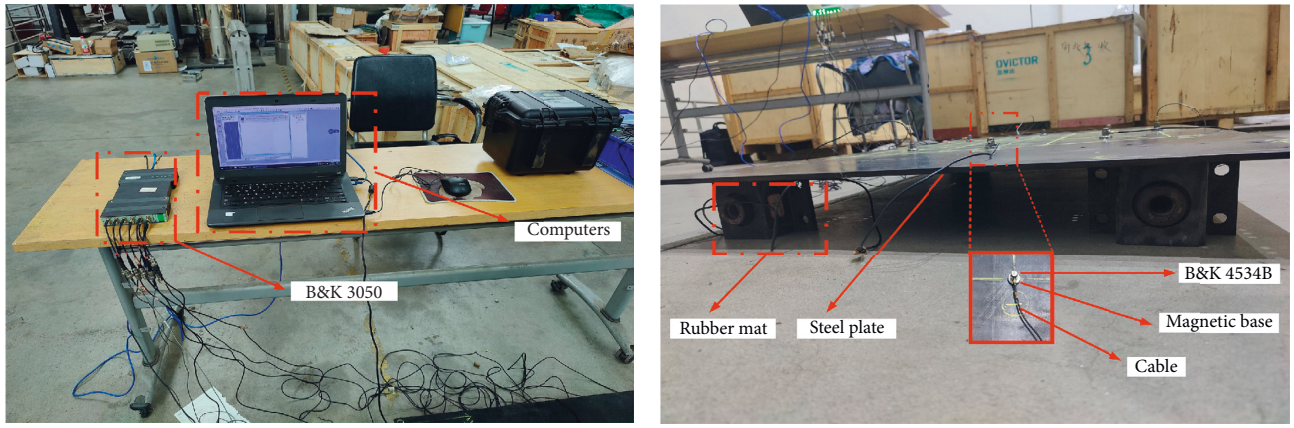

(a) (b)

Figure 5: Setup for impact testing on a flat plate. (a) Data acquisition system. (b) Arrangement of the flat plate and sensors.

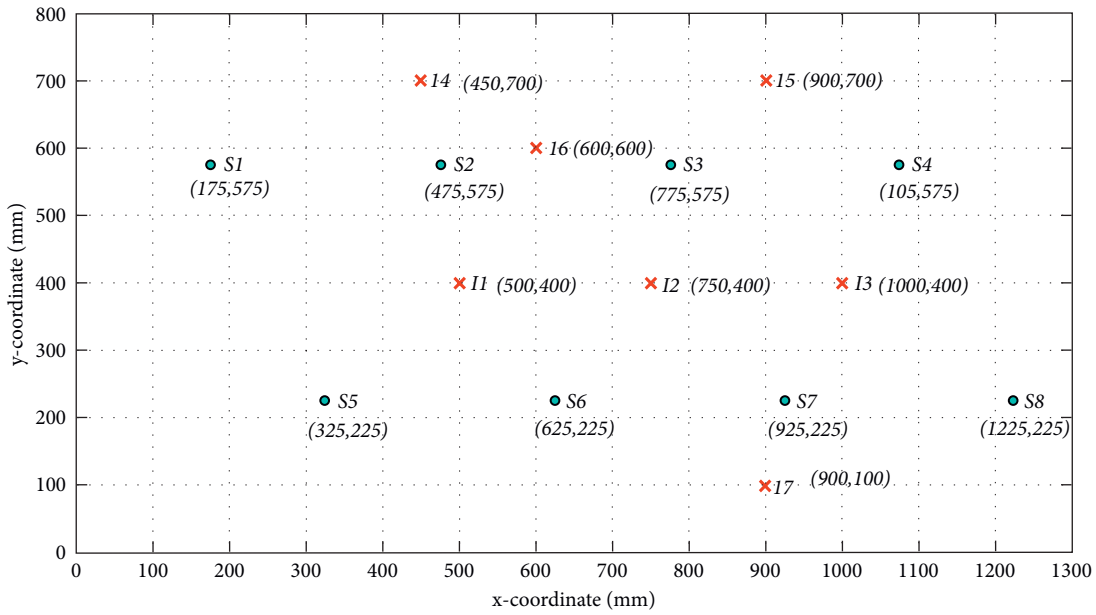

Figure 6: Distribution of sensors and impact points on the flat plate.

$$C\_\text{Error} = \begin{cases} \dfrac{\sqrt{(\Delta\theta \times r)^2 + \Delta z^2}}{\sqrt{(2 \times \pi \times r)^2 + Z^2}} \times 100\%, & |\Delta\theta| \le \pi, \\ \dfrac{\sqrt{(|2\pi - |\Delta\theta|| \times r)^2 + \Delta z^2}}{(2 \times \pi \times r)^2 + Z^2} \times 100\%, & |\Delta\theta| > \pi, \end{cases} \tag{18}$$

where $\Delta\theta$ and Δz denote the difference in the circumferential angle and axial length between the predicted and actual impact points, respectively, and r and Z are the radius and axial length of the cylindrical shell, respectively.

2.6. Impact Test Setup. To evaluate the localization performance of the proposed method, impact tests were performed on the flat plate and cylindrical shell. The test setups used are described next.

2.6.1. Impact Testing on a Flat Plate. A $1300 \times 800 \times 8$-mm flat plate composed of Q235m steel was used for the test. Figure 5(a) shows the data acquisition device and the computers used in the test. A signal generator (B&K 3050) with the sampling rate set to 65536 Hz was used. As shown in Figure 5(b), multiple acceleration sensors (B&K 4534) are connected to the steel plate using a magnetic base. To avoid direct contact between the steel plate and ground, rubber mats were placed under the corners of the plate for vibration isolation.

The impact source was simulated by hitting the plate with a force hammer. The locations of the impact points and the sensors are depicted in Figure 6, where the x- and y-axes are the length and width directions of the plate, respectively,

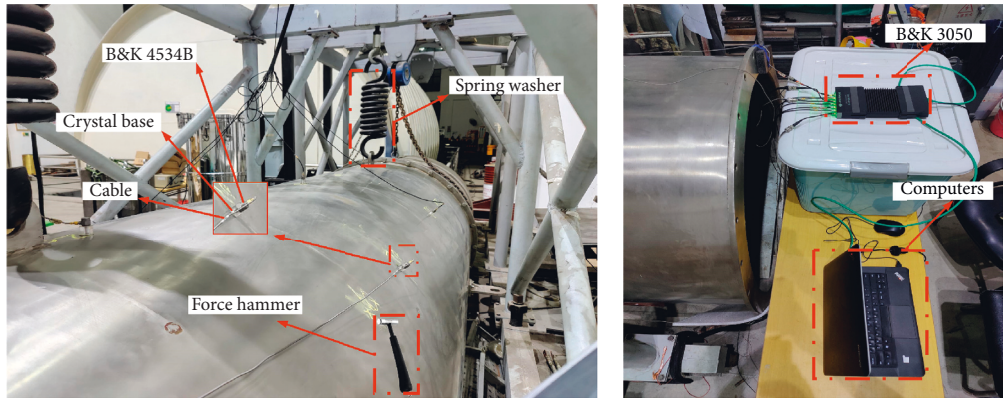

(a) (b)

Figure 7: Setup for impact testing on a cylindrical shell. (a) Arrangement of the cylindrical shell and sensors. (b) Data acquisition system.

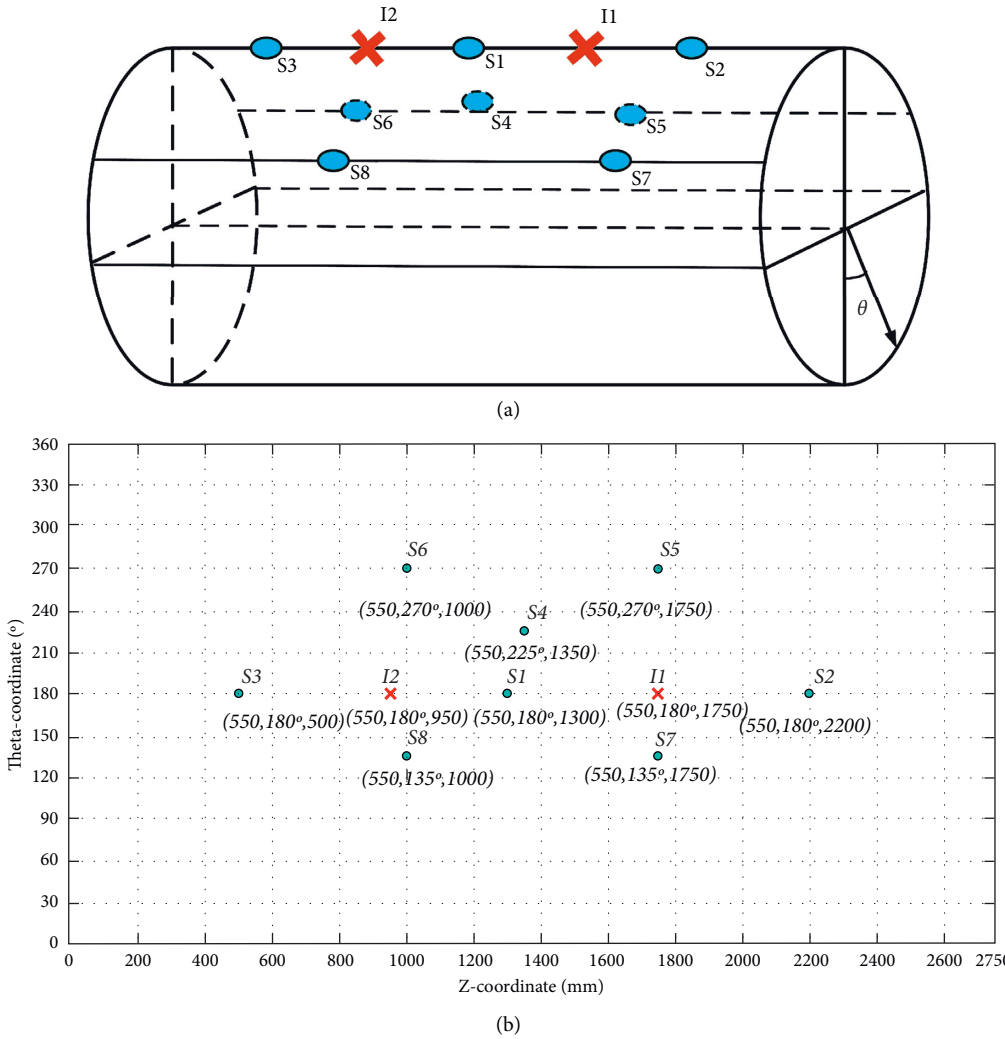

Figure 8: Distribution of sensors and impact points on the cylindrical shell. (a) Three-dimensional diagram of sensor and impact point arrangement. (b) Schematic of the cylindrical housing sensor and impact point plane.

in mm. S1–S8 are the acceleration sensors, denoted by "○"; I1–I7 are the impact points, denoted by "×." The coordinates of the sensor and impact points are marked in the figure (e.g., the coordinates of sensor S1 are (175, 575)). In the test, the impact points were set on the middle and edges of the plate.

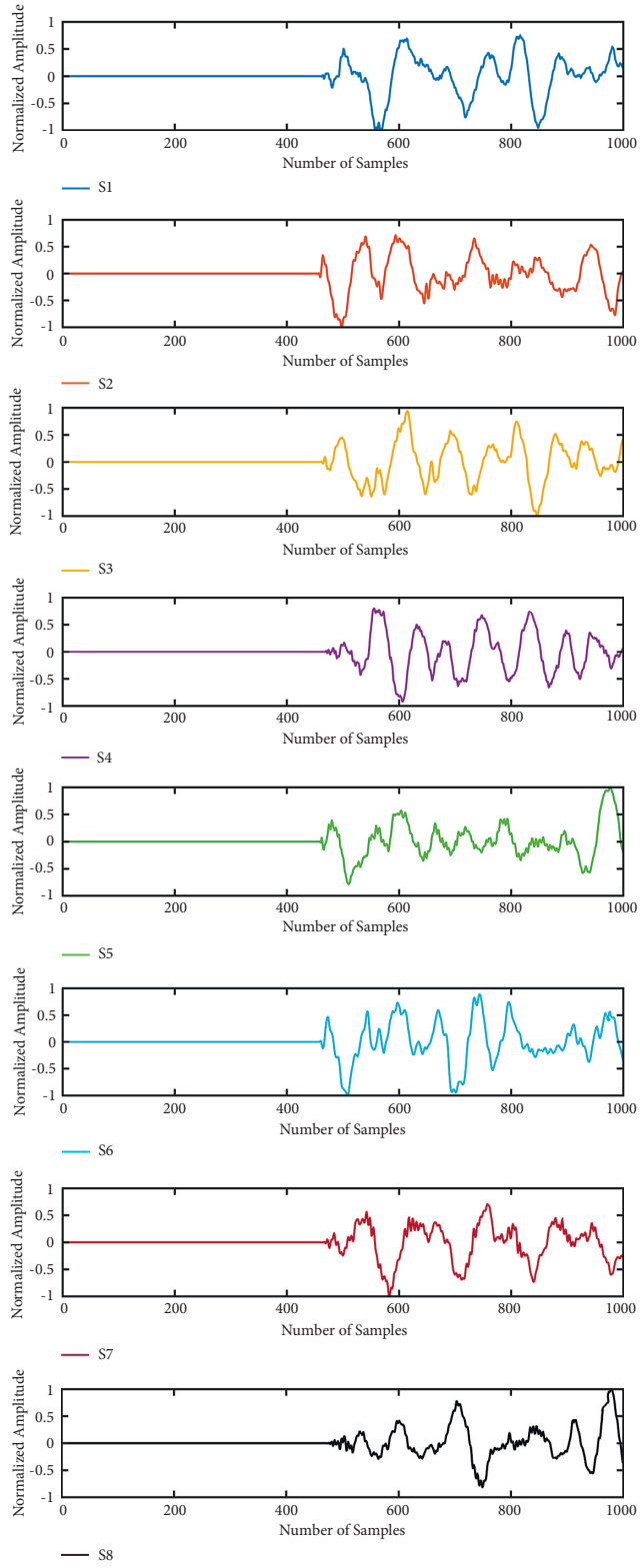

Figure 9: Signals received from sensors S1–S8.

2.6.2. Impact Testing on a Cylindrical Shell. A cylindrical shell with a length of 2750 mm and radius of 550 mm, composed of 304 stainless steel, was used for impact testing. As shown in Figure 7(a), acceleration sensors (B&K 4534) were placed on the outer-surface of the cylindrical shell using a crystal base for connection. The upper part of the cylindrical shell was connected to the test bench through a spring washer to avoid direct contact with the ground.

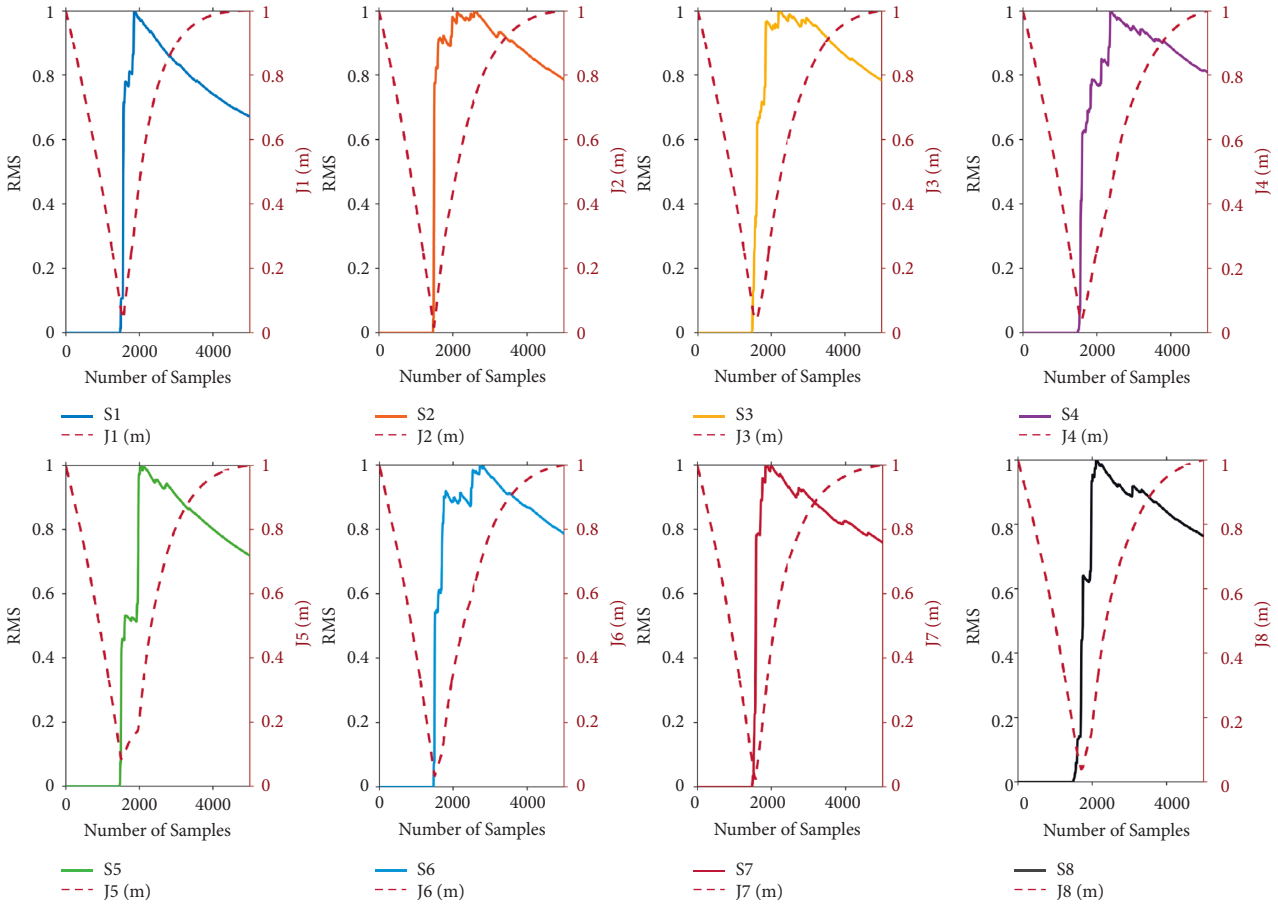

FIGURE 10: RMS and $J(m)$ values of the signals received from sensors S1–S8.

Figure 7(b) shows the data acquisition device and the computers used in the test. A signal generator (B&K 3050) with the sampling rate set to 65536 Hz was used.

As shown in Figure 8, the cylindrical shell was flattened to form a rectangular solid. The horizontal coordinate is the z-axis, which indicates the direction of the length of the cylindrical shell in mm. The vertical coordinate is the θ-axis, which indicates the circumferential angle of the cylindrical shell in degrees. The impact source was again simulated by hitting the shell with a force hammer. The locations of the impact points and sensors are shown in Figure 8. S1–S8 are the acceleration sensors, denoted by "○"; I1–I3 are the impact points, denoted by "×." The coordinates of the sensors and impact points are marked in the figure (e.g., the coordinates of I1 are (550, 225°, 1900), where 550, 225°, and 1900 refer to the radius, circumferential angle, and axial length, respectively).

3. Test Results and Analysis

3.1. Impact Localization on the Flat Plate

3.1.1. Localization Results. Figure 9 shows the normalized impact signal received by acceleration sensors S1–S8 when point I1 is impacted. Equation (8) is used to calculate and normalize the RMS value of each signal. Figure 10 shows the RMS curves and PTOA values of signals received by sensors S1–S8. It can be seen that when the signal does not arrive, the RMS curve of the background noise is in a stable state, and its RMS value is less than 0.0005. Conversely, when the curved wave arrives, its RMS curve starts to rise rapidly and maintains the same growth rate in a short time. PTOA was determined using the dual-RMS algorithm.

All seven impact points (i.e., I1–I7) were located using the proposed algorithm. The results are shown in Figure 11, where the absolute error in the localization distance for each impact point is depicted on top of each image; for example, in Figure 11(a), the absolute localization error is 1.4142 cm. Among the seven points, the localization error is the least at Point I1, with a relative error of only 0.92%; the relative error is maximum (6.58%) at Point I5. In addition, the localization accuracy in the middle of the plate (I1–I3) is significantly higher than that near the edge (I5–I7). This is because when an impact point is located at the edge of the plate, the stress wave generated by the impact is received by the sensor after reflection from the edge. As the waves propagate rapidly, they may overlap at the moment of arrival, resulting in a certain deviation in the PTOA value, degrading the localization accuracy.

Complex background noise is often present in an actual impact monitoring environment. Figure 12 shows the spectrum of the background noise in a real environment,

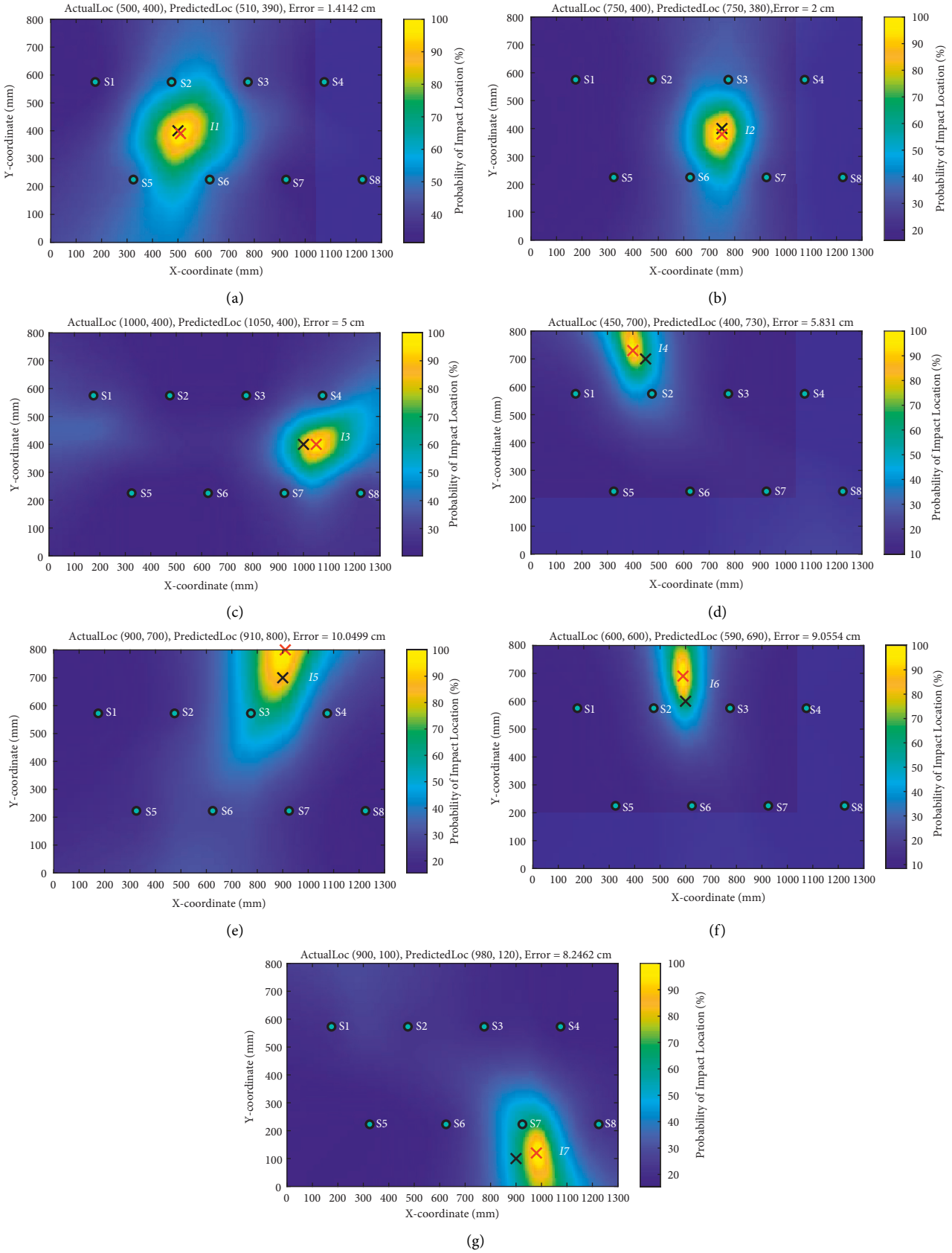

Figure 11: Impact localization results for (a–g) Points I1–17 on the flat plate.

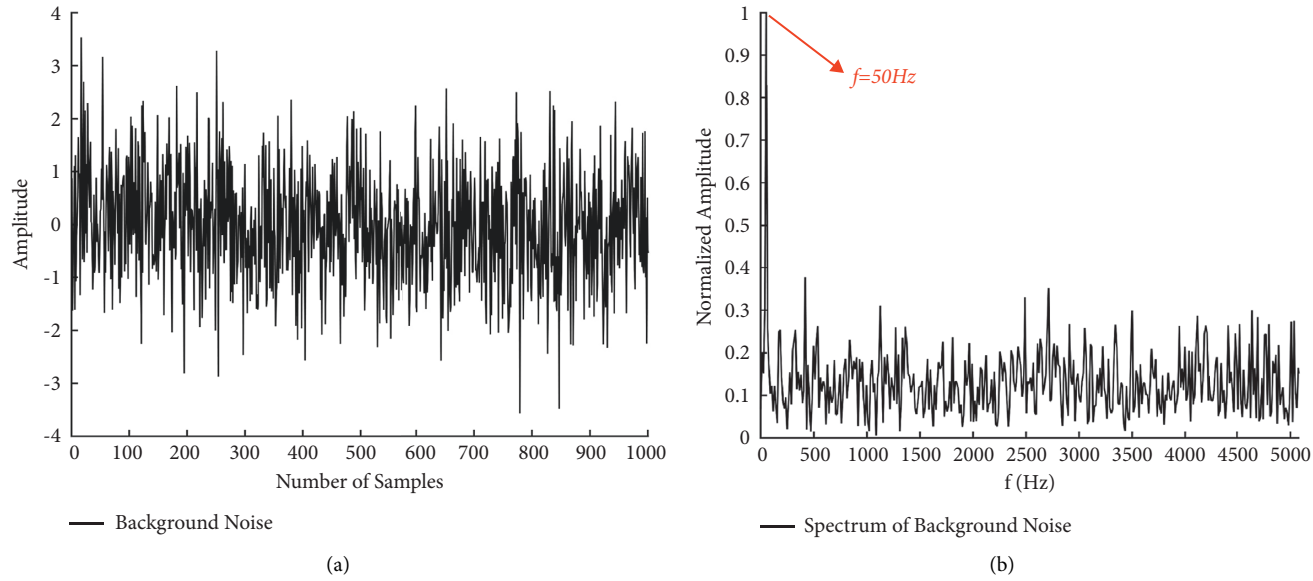

Figure 12: Background noise spectrum. (a) Background noise. (b) Spectrum of background noise.

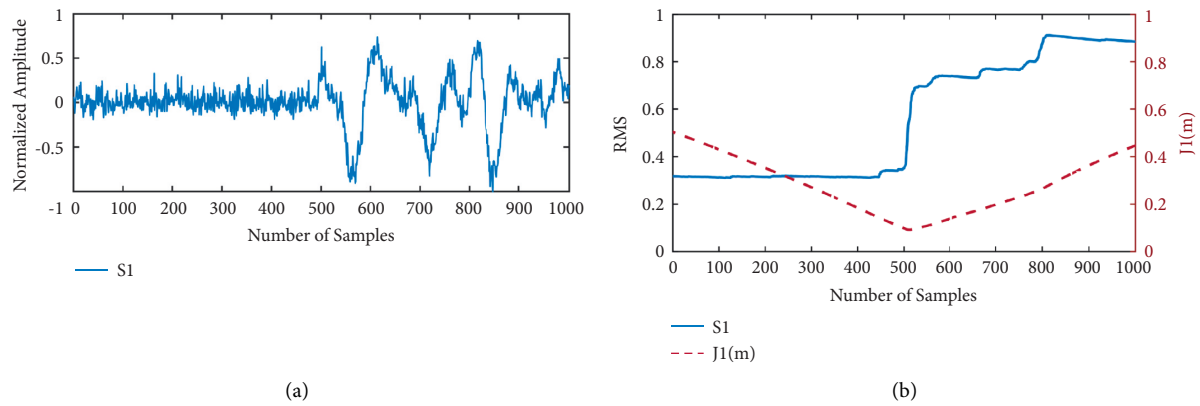

Figure 13: Signal spectrum with added background noise (SNR = 5 dB). (a) Signal from sensor S1. (b) RMS curve of signal and total residual error J(m).

which mainly contains the 50 Hz line spectral frequency and broadband white noise. To further simulate the background noise in a real environment, the impact signals from a real environment were simulated by superimposing background noise. Figure 13(a) displays the signal of sensor S1 superimposed with background noise for Point I1, with a signal-to-noise ratio (SNR) of 5 dB. After adding background noise, it becomes difficult to accurately obtain the initial signal TOA by separating the signal from the noise using the conventional threshold-based approach.

Figure 13(b) shows that the RMS curve of the signal has more energy and fluctuates more when background noise is added. PTOA estimation error will occur if the signal TOA is determined using the fixed-threshold method alone.

Figure 14 shows the localization results for impact points I1–I7 at an SNR of 5 dB. Among these points, the relative localization error is minimum at I3 (0.92%) and maximum at I5 (6.58%). The average localization error for I1–I7 is 3.84%. Furthermore, it can be observed that given the reflection from the boundaries, the localization error for points located in the boundary area is generally greater than that for points farther from the boundary.

Table 1: PTOA difference for each sensor pair for different SNRs at I1.

Sensor pair	No noise	SNR = 5 dB	SNR = 0 dB
S1 & S2	67	68	68
S3 & S4	14	9	13
S5 & S6	8	7	8
S7 & S8	136	136	140

According to equation (13), the localization error is directly affected by the PTOA difference between the signals received from different sensors. Table 1 lists the PTOA difference between four pairs of sensors (S1 & S2, S3 & S4, S5 & S6, and S7 & S8) at different SNRs. The PTOA difference between each sensor pair is very small at different SNRs; for example, for S1 & S2, the difference is only 1.5%. These

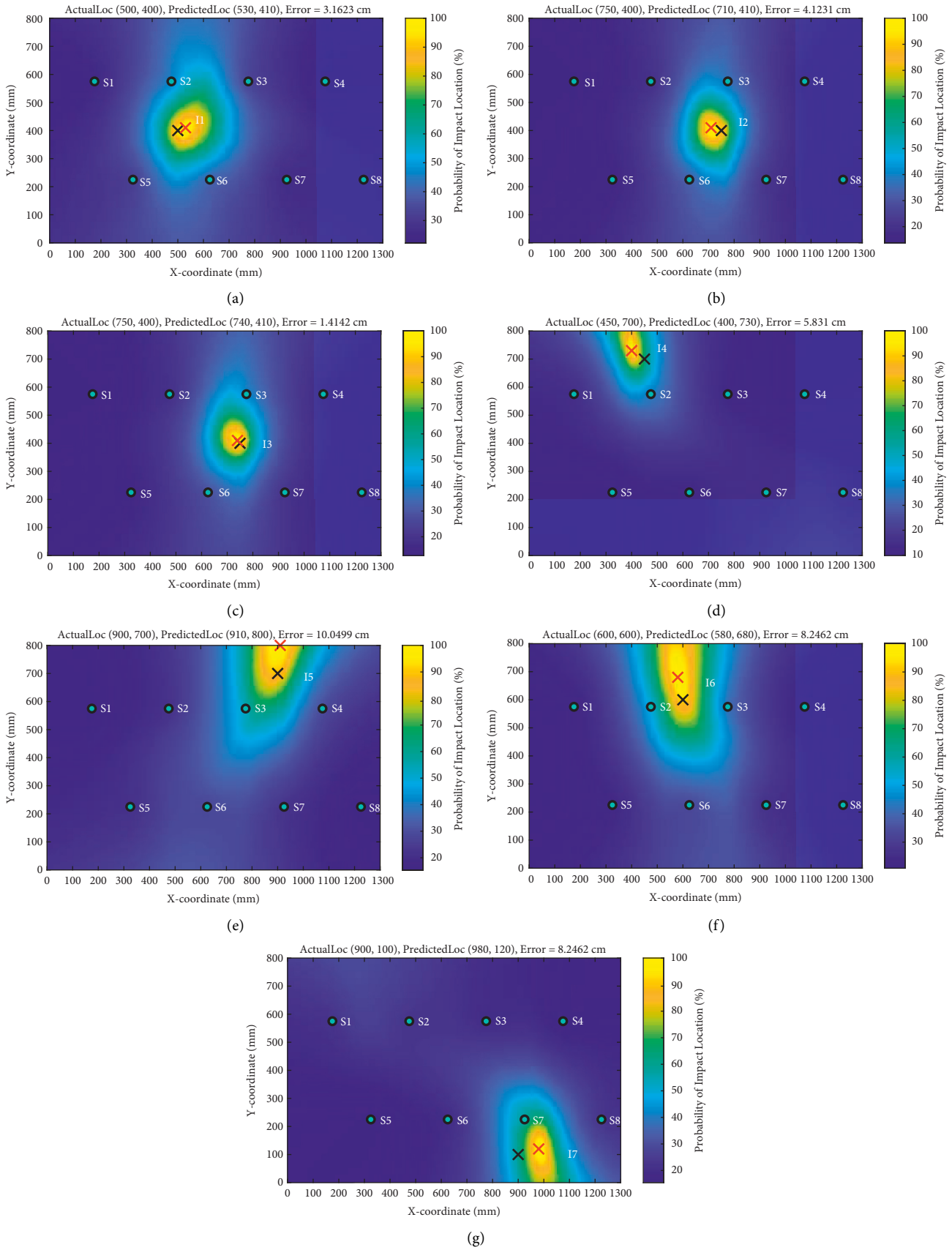

Figure 14: Impact localization results for (a–g) Points I1–I7 with added background noise (SNR = 5 dB).

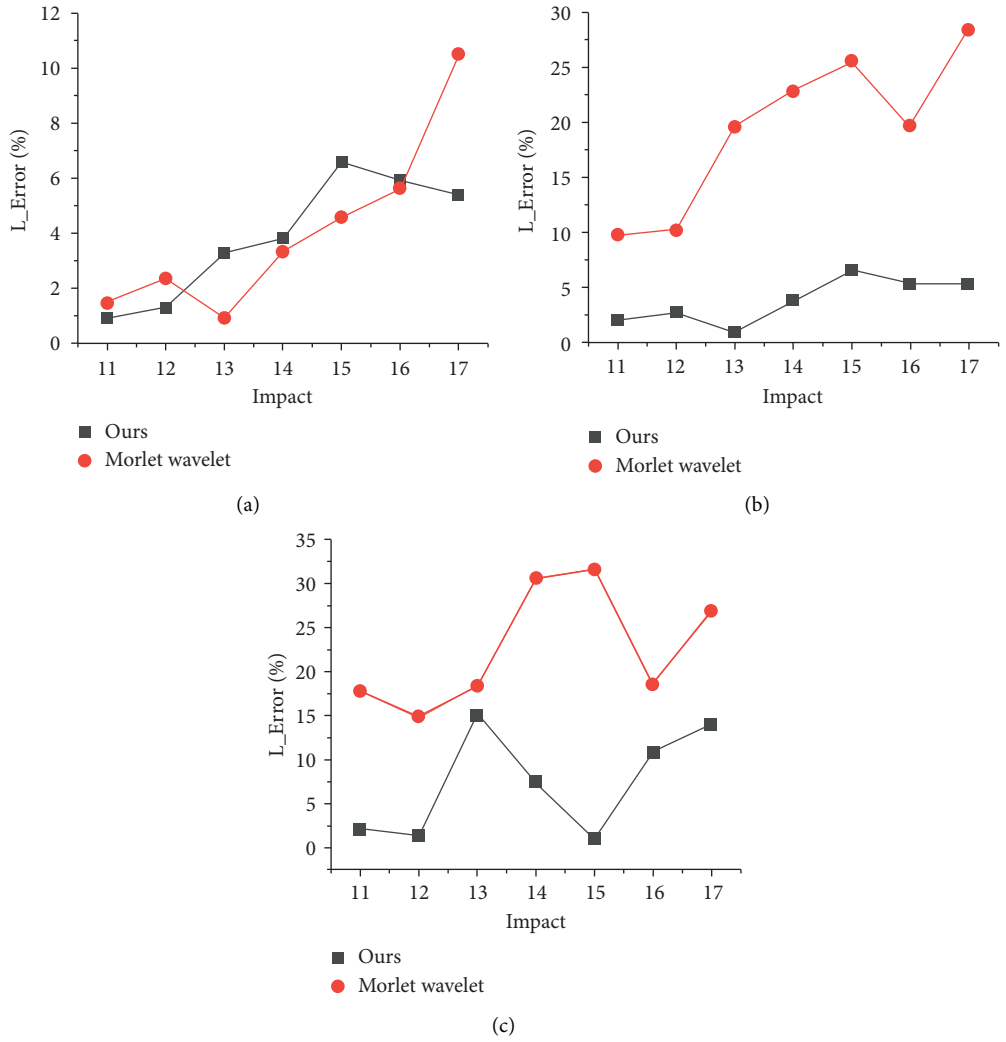

Figure 15: Comparison of the localization errors using the proposed and Morlet wavelet transform algorithms for a flat plate. (a) No noise. (b) SNR = 5 dB. (c) SNR = 0 dB.

results suggest that the proposed method for PTOA estimation is accurate and reliable under background noise interference.

Figure 15 shows the localization error of the proposed algorithm and that of the algorithm for TOA estimation with Morlet wavelet transform [21]. Both algorithms show good localization performance for flat-plate structures without background noise. However, as shown in Figures 15(a) and 15(b), the localization error of our proposed algorithm is significantly less than that of the Morlet wavelet transform algorithm under noisy conditions. At an SNR of 5 and 0 dB, the average localization errors of the proposed algorithm are 15.64% and 15.26% less, respectively, than that of the Morlet wavelet transform algorithm. This suggests that it is difficult to extract the signal TOA using Morlet wavelet transform under noise interference, whereas the proposed algorithm is not affected by background noise interference and can eliminate the influence of noise on TOA estimation utilizing the statistical characteristics of the signal. Furthermore, the proposed algorithm can adapt to different working conditions because the threshold does not need to be predetermined based on empirical experience.

3.2. Impact Localization on the Cylindrical Shell

3.2.1. Impact Localization Results. Figure 16 shows the impact localization results for the cylindrical shell structure using the proposed algorithm described in Section 2.2. The maximum localization error is at Point I1 (7.24%), and the minimum localization error is at Point I2 (1.75%), with an average localization error of 3.25%. These results demonstrate that the proposed impact localization algorithm can be used to accurately locate the impact points on cylindrical shell structures.

3.2.2. Influence of Background Noise on Impact Localization. The same background noise is superimposed on the sensor receiving signals arranged on the cylindrical shell. When the impact point is far from the sensor, the impact signal rapidly

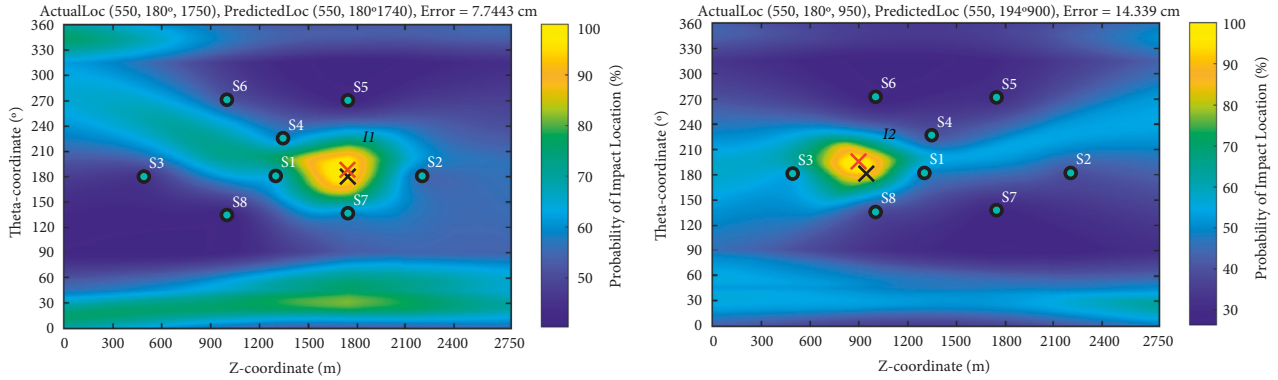

Figure 16: Impact locations on the cylindrical shell. (a) I1. (b) I2.

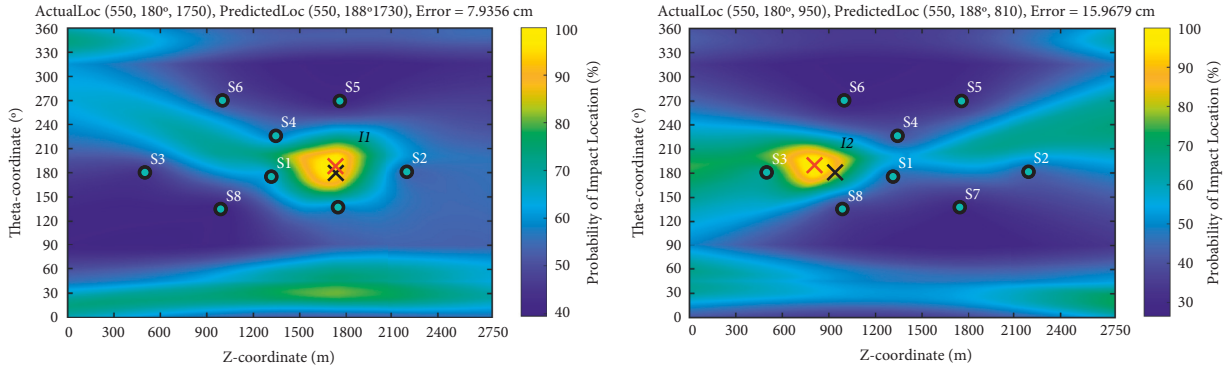

Figure 17: Impact locations on the cylindrical shell for SNR = 5 dB. (a) I1. (b) I2.

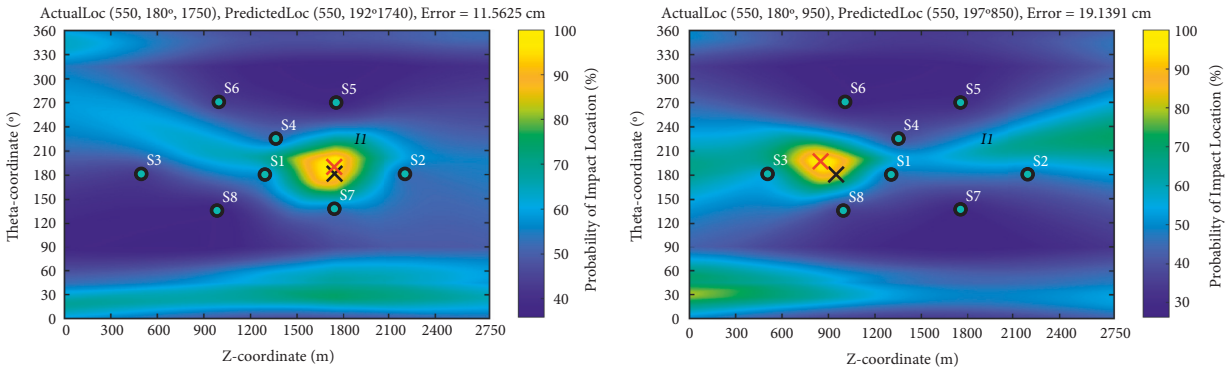

Figure 18: Impact locations on the cylindrical shell for SNR = 0 dB. (a) I1. (b) I2.

attenuates. Figures 17 and 18 show the impact localization results under different noise conditions (SNR = 5 and 0 dB, respectively). Under both conditions, the localization error does not exceed 5%, demonstrating that the localization algorithm for the cylindrical shell is not highly affected by noise interference and can achieve good localization results. For the cylindrical shell structure, the proposed and Morlet wavelet algorithms were compared in terms of the relative

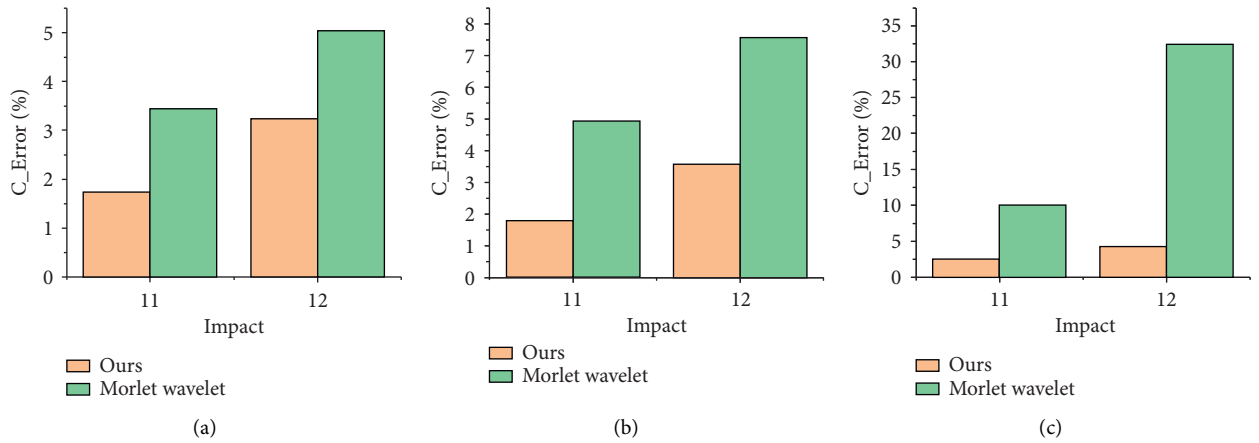

Figure 19: Localization error comparison using the proposed and Morlet wavelet transform algorithms for a cylindrical shell. (a) No noise. (b) SNR = 5 dB. (c) SNR = 0 dB.

localization error; the results are depicted in Figure 19. The proposed algorithm has lesser localization error compared to the Morlet wavelet algorithm. Under different noise conditions (i.e., no noise, and SNR = 5 and 0 dB), the mean relative error is improved by 1.8%, 3.97%, and 28.12%, respectively, with the proposed algorithm. These results suggest that the proposed algorithm can achieve satisfactory results for impact localization on cylindrical shell structures.

4. Conclusions

This article presents an error-index-based low-speed impact location algorithm, which is suitable not only for a flat plate but also for cylindrical shell structures. First, a dual-RMS algorithm based on signal energy characteristics is proposed to estimate the TOA of signals. This algorithm is adaptive and does not require complex signal processing and artificial threshold setting. The probability function is constructed by introducing an error index to map the impact location. The percussion test results on a flat plate and cylindrical shell demonstrate the following:

(1) The dual-RMS algorithm can accurately and stably estimate the TOA difference of bending waves under noise interference.

(2) The proposed positioning algorithm has a good positioning effect on both flat plate and cylindrical shell structures. Under no noise conditions and for SNR = 5 and 0 dB, the average relative error ratio of the Morlet wavelet algorithm is improved by 0.22%, 15.64%, and 15.26%. For the cylindrical shell structure, the average relative errors increase by 1.8%, 3.97%, and 28.12%. It can be seen that the proposed algorithm has a good application value for low-speed impact location on large structures under low-SNR conditions.

(3) In the flat-plate test, it is verified that the location error of the percussion point at the edge of the plate structure is generally greater than that of the middle position due to the influence of boundary reflection. In future work, the edge location algorithm should be improved to reduce the impact of boundary reflection.

Data Availability

The data supporting the findings of this study are available from the corresponding author upon reasonable request.

Conflicts of Interest

The authors declare that there are no conflicts of interest regarding the publication of this article.

Acknowledgments

This work was supported by this project (4142Z3391233).

References

[1] A. H. Baluch, O. Falcó, J. L. Jiménez, B. H. A. H. Tijs, and C. S. Lopes, "An efficient numerical approach to the prediction of laminate tolerance to barely visible impact damage," *Composite Structures*, vol. 225, p. 111017, 2019.

[2] G. Lu, Y. Zhou, and Y. Xu, "Low velocity impact localization of variable thickness composite laminates," *Sensors*, vol. 21, no. 18, p. 6103, 2021.

[3] B. Sasikirono, S. J. Kim, G. D. Haryadi, and A. Huda, "Risk analysis using corrosion rate parameter on gas transmission pipeline," *IOP Conference Series: Materials Science and Engineering*, vol. 202, p. 012099, 2017.

[4] B. Chen, C. Hei, M. Luo, M. S. C. Ho, and G. Song, "Pipeline two-dimensional impact location determination using time of arrival with instant phase (TOAIP) with piezoceramic transducer array," *Smart Materials and Structures*, vol. 27, no. 10, p. 105003, 2018.

[5] M. T. Martin and J. F. Doyle, "Impact force location in frame structures," *International Journal of Impact Engineering*, vol. 18, no. 1, pp. 79–97, 1996.

[6] Y. Ren, L. Qiu, S. Yuan, and Z. Su, "A diagnostic imaging approach for online characterization of multi-impact in aircraft composite structures based on a scanning spatial-

wavenumber filter of guided wave," *Mechanical Systems and Signal Processing*, vol. 90, pp. 44–63, 2017.

[7] S. Yu, C. Fan, and Y. Zhao, "Hypervelocity impact detection and location for stiffened structures using a probabilistic hyperbola method," *Sensors*, vol. 22, no. 8, p. 3003, 2022.

[8] V. La Saponara, D. A. Horsley, and W. Lestari, "Structural health monitoring of glass/epoxy composite plates using PZT and PMN-PT transducers," *Journal of Engineering Materials and Technology*, vol. 133, no. 1, 2010.

[9] F. Ciampa and M. Meo, "Acoustic emission source localization and velocity determination of the fundamental mode A0using wavelet analysis and a Newton-based optimization technique," *Smart Materials and Structures*, vol. 19, no. 4, p. 045027, 2010.

[10] J. Frieden, J. Cugnoni, J. Botsis, and T. Gmür, "Low energy impact damage monitoring of composites using dynamic strain signals from FBG sensors - Part I: impact detection and localization," *Composite Structures*, vol. 94, no. 2, pp. 438–445, 2012.

[11] Y. Sai, M. Jiang, Q. Sui, S. Lu, and L. Jia, "Multi-source acoustic emission localization technology research based on FBG sensing network and time reversal focusing imaging," *Optik*, vol. 127, no. 1, pp. 493–498, 2016.

[12] M. Jiang, Y. Sai, X. Geng, Q. Sui, X. Liu, and L. Jia, "Development of an FBG sensor array for multi-impact source localization on CFRP structures," *Sensors*, vol. 16, no. 10, p. 1770, 2016.

[13] L.-X. Fang, D.-S. Zhao, T.-T. Ji, F. Zeng, and W. Zhang, "Loose parts localization delay calculation method based on CWT and Hilbert envelope," *Nuclear Technology*, vol. 193, no. 2, pp. 276–286, 2016.

[14] Z. Matousek, M. Babjak, and J. Ochodnicky, "Correlation-based TDOA algorithm for the target localization at low signal to noise ratio," in *In Proceedings of the 2016 New Trends in Signal Processing (NTSP)*, Demanovska Dolina, Slovakia, October 2016.

[15] D. E. Norwood, E. Simpson, and S. M. Mahajan, "Impact identification using matched filtering and spectral cross correlation," in *Proceedings of IEEE Southeastcon*, Jacksonville, FL, USA, April 2013.

[16] G. C. McLaskey, S. D. Glaser, and C. U. Grosse, "Beamforming array techniques for acoustic emission monitoring of large concrete structures," *Journal of Sound and Vibration*, vol. 329, no. 12, pp. 2384–2394, 2010.

[17] C. Chen, Y. Chen, Y. Han, H.-Q. Lai, and K. J. R. Liu, "High resolution carrier frequency offset estimation in time-reversal wideband communications," *IEEE Transactions on Communications*, vol. 66, no. 5, pp. 2191–2205, 2018.

[18] T. S. Papulak, *An Inverse Acoustical Phased Array Technique for Impact Detection and Location*, Dissertation, University of Utah, Salt Lake City, Utah, USA, 2012.

[19] T. He, Y. Xie, Y. Shan, and X. Liu, "Localizing two acoustic emission sources simultaneously using beamforming and singular value decomposition," *Ultrasonics*, vol. 85, pp. 3–22, 2018.

[20] L. Qiu, S. Yuan, X. Zhang, and Y. Wang, "A time reversal focusing based impact imaging method and its evaluation on complex composite structures," *Smart Materials and Structures*, vol. 20, no. 10, p. 105014, 2011.

[21] D. Pang, Q. Sui, Y. Wang, R. Sun, R. Wang, and Y. Wang, "Acoustic emission source localization system using fiber Bragg grating sensors and a barycentric coordinate-based algorithm," *Journal of Sensors*, vol. 2018, Article ID 9053284, 1–8 pages, 2018.

[22] Z. Wu, L. Xu, Y. Wang, and Y. Cai, "Impact energy identification on a composite plate using basis vectors," *Smart Materials and Structures*, vol. 24, no. 9, p. 095007, 2015.

[23] S. K. Al-Jumaili, M. R. Pearson, K. M. Holford, M. J. Eaton, and R. Pullin, "Acoustic emission source location in complex structures using full automatic delta T mapping technique," *Mechanical Systems and Signal Processing*, vol. 72-73, no. 73, pp. 513–524, 2016.

[24] I. Tabian, H. Fu, and Z. S. Khodaei, "A convolutional neural network for impact detection and characterization of complex composite structures," *Sensors*, vol. 19, no. 22, p. 4933, 2019.

[25] M. S. Hossain, Z. C. Ong, S. C. Ng, Z. Ismail, and S. Y. Khoo, "Inverse identification of impact locations using multilayer perceptron with effective time-domain feature," *Inverse Problems in Science and Engineering*, vol. 26, no. 3, pp. 443–461, 2017.

[26] Z. Sharif-Khodaei and M. H. Aliabadi, "Impact detection and identification with piezoceramic sensors: passive sensing," *Computational and Experimental Methods Series*, pp. 215–265, 2017.

[27] J. Haywood, P. T. Coverley, W. J. Staszewski, and K. Worden, "An automatic impact monitor for a composite panel employing smart sensor technology," *Smart Materials and Structures*, vol. 14, no. 1, pp. 265–271, 2004.

[28] A. De Luca, D. Perfetto, G. Lamanna, A. Aversano, and F. Caputo, "Numerical investigation on guided waves dispersion and scattering phenomena in stiffened panels," *Materials*, vol. 15, no. 1, p. 74, 2021.

[29] R. Gorgin, Z. Wang, Z. Wu, and Y. Yang, "Probability based impact localization in plate structures using an error index," *Mechanical Systems and Signal Processing*, vol. 157, Article ID 107724, 2021.

[30] L. Qi, Z. Zeng, L. Sun et al., "An impact location algorithm for spacecraft stiffened structure based on posterior possibility correlation," *Sensors*, vol. 20, no. 2, p. 368, 2020.

[31] T. Manco, J. P. Martins, C. Rigueiro, and S. L. Simões-da-Silva, "Ultimate resistance of isotropic cylindrically curved steel panels under uniaxial compression," *Journal of Constructional Steel Research*, vol. 159, pp. 95–108, 2019.

[32] Y. Zhang, "CWT-based method for extracting seismic velocity dispersion," *IEEE Geoscience and Remote Sensing Letters*, vol. 19, no. 1–5, pp. 1–5, 2022.

[33] A. G. Every, "Intersections of the lamb mode dispersion curves of free isotropic plates," *Journal of the Acoustical Society of America*, vol. 139, no. 4, pp. 1793–1798, 2016.

[34] R. Killick, P. Fearnhead, and I. A. Eckley, "Optimal detection of changepoints with a linear computational cost," *Journal of the American Statistical Association*, vol. 107, no. 500, pp. 1590–1598, 2012.

[35] S. Wang, H. Wang, D. Wang et al., "AE source localization and imaging on cylindrical shell structures based on six-Ae-sensor monitoring network and VTR focusing imaging," *Nondestructive Testing and Evaluation*, vol. 36, no. 1, pp. 35–61, 2019.